Journal of Environmental Chemical Engineering 10 (2022) 107425

Contents lists available at ScienceDirect

Journal of Environmental Chemical Engineering

journal homepage: www.elsevier.com/locate/jece

Effect of Mg^{2+}-, Sr^{2+}-, and Fe^{3+}-substitution on ^{85}Sr and ^{60}Co adsorption on amorphous calcium phosphates: Adsorption performance, selectivity, and mechanism

Andrei Ivanets [a,*], Aleksej Zarkov [b], Vladimir Prozorovich [a], Ekaterina Venhlinskaya [c], Artsiom Radkevich [c], Jen-Chang Yang [d], Evgeniy Papynov [e], Sofiya Yarusova [f,g], Aivaras Kareiva [b]

[a] Institute of General and Inorganic Chemistry of National Academy of Sciences of Belarus, st. Surganova 9/1, 220072 Minsk, Belarus
[b] Institute of Chemistry, Vilnius University, Naugarduko 24, LT-03225 Vilnius, Lithuania
[c] Joint Institute for Power and Nuclear Research–Sosny of the National Academy of Sciences of Belarus, PO Box 119, Minsk BY-220109, Belarus
[d] Graduate Institute of Nanomedicine and Medical Engineering, College of Biomedical Engineering, Taipei Medical University, 250 Wu-Hsing St, Taipei 11052, Taiwan
[e] Far Eastern Federal University, 10 Ajax Bay, Russky Island, 690922, Vladivostok, Russia
[f] Institute of Chemistry, Far Eastern Branch of Russian Academy of Sciences, 159, Prosp. 100-letiya Vladivostoka, Vladivostok 690022, Russia
[g] Vladivostok State University of Economics and Service, Gogolya st., 41, Vladivostok 690014, Russia

ARTICLE INFO

Editor: Kaimin Shih

Keywords:
Amorphous calcium phosphate
Metal-substituted calcium phosphate
^{85}Sr and ^{60}Co adsorbents
Liquid radioactive waste
Dissolution-precipitation mechanism

ABSTRACT

Hydroxyapatite $Ca_{10}(OH)_2(PO_4)_6$ is a well-known efficient adsorbent of dyes, heavy metal ions, and radionuclides. Its adsorption efficacy strongly depends on crystalline/amorphous structure, defectiveness, texture characteristics, and morphology. Herein, we synthesized Mg^{2+}-, Sr^{2+}-, and Fe^{3+}-substituted (5 mol%) amorphous calcium phosphates as an effective ^{85}Sr and ^{60}Co radionuclides adsorbents. The introduction of Mg^{2+}-, Sr^{2+}-, and Fe^{3+} ions led to the formation of amorphous calcium phosphates with particles size in the nanoscale range of approximately 10–50 nm. The features of the adsorption behavior of amorphous calcium phosphates were determined depending on the variation of the pH of aqueous, NaCl and $CaCl_2$ solutions. Fe^{3+}-substituted samples demonstrated the superior adsorption efficiency to ^{85}Sr (K_d 7.77 $\times 10^3$ cm^3/g) and ^{60}Co (K_d 6.84 $\times 10^4$ cm^3/g) radionuclides at pH of 10.0 and 4.0, respectively. The adsorption performance of obtained adsorbents slowly decreased at 0.1 M NaCl backgrounds and K_d ^{85}Sr and ^{60}Co reached 1.67 $\times$ 10^3 and 2.78 $\times$ 10^4 cm^3/g for non-substituted calcium phosphate. The dramatic decrease of calcium phosphates adsorbents efficiency to ^{85}Sr (K_d <150 cm^3/g) and ^{60}Co (K_d $<1.34 \times 10^3$ cm^3/g) for 0.05 M $CaCl_2$ model solution was established. The adsorption mechanism of dissolution-precipitation (for ^{85}Sr) and chemisorption (for ^{60}Co) was proposed. Fe^{3+}-substituted calcium phosphate showed the competitive affinity and selectivity to ^{85}Sr and ^{60}Co comparing with described inorganic adsorbents and to be considered as prospective adsorbent for wastewater treatment in nuclear industry.

1. Introduction

Hydroxyapatite (HAp), due to its low solubility, good ion-exchange characteristics and developed porous structure, is widely used in biomedical applications [1–3], for targeted drug delivery [4,5], as well as an adsorbent for a wide range of toxic pollutants (dyes, heavy metal ions, radionuclides) [6–9]. The adsorption properties of calcium phosphates significantly depend on various factors, including the crystalline and porous structure, the presence of defects and amorphous inclusions, the morphology of particles, etc. [10,11]. These characteristics can be purposefully varied at the synthesis stage. At the same time, the synthesis method, the reagents concentration, the medium pH, the synthesis duration, as well as hydrothermal treatment, exposure to ultrasonic or microwave radiation were widely studied for the production of calcium phosphates with specified physical-chemical properties [12–15].

One of the effective approaches to the directed regulation of the structure and adsorption properties of HAp is the introduction of dopant ions into its composition [16]. It is known that Mg^{2+} ions, due to their

* Corresponding author.
E-mail addresses: ivanets@igic.bas-net.by, andreiivanets@yandex.ru (A. Ivanets).

https://doi.org/10.1016/j.jece.2022.107425
Received 16 October 2021; Received in revised form 13 February 2022; Accepted 15 February 2022
Available online 17 February 2022

ability to be adsorbed on the surface of calcium phosphate nuclei, are effective crystallization inhibitors, which lead to the formation of amorphous compounds with a high specific surface [17,18]. The influence of the peculiarities of HAp crystallization in the presence of magnesium ions is especially important to take into account when forming it for bone engineering and using it for modifying the implant surface [19]. In addition, a number of authors have studied the effect of the introduction of magnesium ions into the structure of calcium phosphates on the efficiency of adsorption of heavy metal ions. It was shown that Mg-substituted samples had a higher capacity of lead, cadmium, copper, etc. [20,21].

It is also important to understand the regularities of HAp interaction with Sr^{2+} ions, as well as the processes occurring during the formation of Sr-substituted HAp. This is due to the similarity of the chemical properties of calcium and strontium ions, which can lead to the substitution of Ca^{2+} for Sr^{2+} ions by an ion-exchange mechanism [22]. The course of this reaction when strontium radionuclides enter a living organism leads to negative consequences, rapid development of osteochondrosis, as well as irreversible destruction of bones. In addition to reducing the mechanical strength of bone tissue, the replacement of calcium with radiostrontium leads to constant irradiation of nearby organs with radiation [23]. In a number of works, an attempt was made to immobilize the radionuclide ^{90}Sr during the deposition of HAp in solutions of liquid radioactive waste. The effectiveness of this approach is shown, and it is also proposed to carry out the subsequent immobilization of ^{90}Sr by heat treatment of the deposited Sr-substituted HAp [24,25].

Of particular interest to researchers is the production of HAp composites with iron oxides [26,27]. This is due to the fact that these materials have excellent magnetic characteristics, which is used in magnetic resonance therapy [28], targeted drug delivery [29], as well as for magnetic separation of spent adsorbents [30–32]. In addition to giving new functional properties, it is believed that calcium ions can be replaced by iron ions in the interparticle contacts of the composite, which affects the solubility of HAp, and as a result, the adsorption properties [33]. At the same time, the reviews widely describe the most diverse composition of HAp composites with iron oxides. However, the regularities of obtaining Fe-substituted calcium phosphates have been studied in fragments and require systematic research.

In this work, we synthesized Mg^{2+}-, Sr^{2+}-, and Fe^{3+}-substituted amorphous calcium phosphates (ACPs). The work aimed to study the effect of the introduced dopant ions on the structure and adsorption properties of calcium phosphates to ^{85}Sr and ^{60}Co radionuclides. As the above literature review showed, there have been no systematic studies on the effect of Mg^{2+}-, Sr^{2+}-, and Fe^{3+} dopants on the radionuclides adsorption on calcium phosphates. Thus, firstly the following were studied: (i) physical-chemical properties and structure of metal-substituted calcium phosphates; (ii) the effect of pH, NaCl and $CaCl_2$ salt background on the adsorption and selective properties of the obtained adsorbents; (iii) a mechanism for the ^{85}Sr and ^{60}Co radionuclides removal from solutions was proposed.

2. Experimental

2.1. Synthesis of M-substituted calcium phosphates

Calcium nitrate tetrahydrate ($Ca(NO_3)_2{\bullet}4H_2O$, ≥ 99%, Roth), magnesium nitrate hexahydrate ($Mg(NO_3)_2{\bullet}6H_2O$, 99%, Chempur), strontium nitrate ($Sr(NO_3)_2$, ≥ 99%, Roth), iron(III) nitrate nonahydrate ($Fe(NO_3)_3{\bullet}9H_2O$, ≥ 98%, Sigma-Aldrich) and diammonium hydrogen phosphate ($(NH_4)_2HPO_4$, ≥ 98%, Roth) were used as starting materials. Synthesis of pristine and metal-substituted ACPs with substitution level of 5 mol% was performed by previously reported procedure [34,35]. Substitution level by foreign ions is given here with respect to Ca^{2+} ions. Firstly, an appropriate amount of $(NH_4)_2HPO_4$ was dissolved in deionized water to obtain a 0.5 M solution, to which concentrated ammonia solution (NH_4OH, 25%, Roth) was added under constant mixing in order to adjust the pH value to 10. Next, an aqueous solution containing appropriate metal nitrates (total metal ions concentration was 0.75 M) was rapidly added to the above mixture. The instant formation of precipitates was observed, which were aged in the reaction mixture for 10 min, afterwards filtered, washed with 100 mL of each deionized water and ethanol, and dried at 50 °C overnight in the oven.

2.2. Physical-chemical methods

Powder X-ray diffraction data were collected using Ni-filtered Cu Kα radiation on Rigaku MiniFlex II diffractometer working in Bragg-Brentano (θ/2θ) geometry. The data were collected within 2θ angle range from 10° to 60° at a step width of 0.02° and speed of 1°/min. Infrared (FTIR) spectra were obtained in the range of 4000–400 cm^{-1} employing Bruker ALPHA ATR spectrometer. Morphological features and elemental composition of powders were studied by scanning electron microscopy performed with a Hitachi SU-70 field-emission scanning electron microscope (FE-SEM) and energy dispersive X-ray spectroscopy (EDX). Elemental analysis of ACPs was performed by means of inductively coupled plasma optical emission spectrometry (ICP-OES) using Perkin Elmer Optima 7000DV spectrometer. The samples prior to analysis were dissolved in 5% nitric acid (HNO_3, Rotipuran® Supra 69%, Roth) and diluted to an appropriate volume with deionized water. Calibration solutions were prepared by dilution of the stock standard solutions (single-element ICP standards 1000 mg/L, Roth). The pH drift method was applied for the estimation of the zero point charge (pH_{zpc}) of ACPs. The pH_{zpc} was determined by the point of interaction of lines pH_{final} and $pH_{initial}$ as function of $pH_{initial}$.

2.3. Batch ^{85}Sr and ^{60}Co adsorption experiment

The hydrolytic stability of calcium phosphates in aqueous solutions was studied in a wide pH range and in the presence of NaCl and $CaCl_2$ electrolytes was in depth studied previously [36]. It was shown that tricalcium phosphate is stable at pH 4.5–10.0, and hydroxyapatite, at pH 3.0–12.0. An increase in the ratio of the solution volume to the weight of phosphates from 250 to 500 mL/g leads to an increase in the degree of hydrolysis by a factor of 1.4–1.9. In the presence of 0.01 M NaCl and 0.001 M $CaCl_2$, all samples exhibit high hydrolytic stability. The obtained results were considered for choice the adsorption experiment conditions.

The model solutions of liquid radioactive waste were prepared using distilled water, as well as background electrolytes (0.1 M NaCl and 0.01 M $CaCl_2$), followed by adjustment of solutions pH on the pH-meter I-160 (ZIP, Belarus). The initial activity of ^{85}Sr and ^{60}Co radionuclides for adsorption experiments was 100 ± 30 kBq/L of each radionuclide. The effect of pH was studied in the range of 4.0, 7.0, 10.0. The required pH value was adjusted by adding of HCl or NaOH solutions. The adsorbent samples at V (solution)/m (adsorbent) ratio of 500 mL/g was used for all experiments. The adsorbent was cautiously stirring with model solutions by shaker at 250 rpm during 24 h.

The radionuclides activity in the solution before (A_0, kBq/L) and after adsorption in analyzed aliquot (A, kBq/L) was measured by MKSAT1315 γ, β-spectrometer (Atomtex, Belarus). The removal efficiency (α) and distribution coefficient (K_d) were calculated using the Eqs. (1) and (2). Samples were taken every 10–20 mL, followed by measuring their activity

$$\alpha = \left(A_0 - A_{eq}\right)/A_0 \quad (1)$$

$$K_d = \frac{A_0 - A_{eq}}{A_{eq}} \times \frac{V}{m} \quad (2)$$

where A_0, A_{eq} – initial and equilibrium specific activity, kBq/L; V – volume of solution, cm^3; m – mass of sorbent, g.

All adsorption study was performed in triple parallel experiments

and the average values were used. The standard deviation for the radionuclides activity measuring and K_d values calculations did not exceed 5%.

3. Results and discussion

3.1. Adsorbents characterization

The XRD patterns of as-prepared pristine and ion-substituted ACPs are demonstrated in Fig. 1(a). It is obvious, that all powders possessed amorphous nature reflected in a very broad signal centered at the same position at around 30 degrees regardless of ionic substitution, which is characteristic of ACP [37]. There were no sharp diffraction peaks, which could be ascribed to crystalline phases. The obtained results clearly indicated that ion-substitution did not affect crystallinity of the samples.

Fig. 1(b) shows the FTIR spectra of pristine and ion-substituted ACP in the representative spectral rage of 1800–400 cm^{-1}. In all cases, the most dominant resonance of the analyzed samples are the phosphate ν_3 mode and the phosphate ν_4 domain, centered at 1020 and 550 cm^{-1}, respectively [4]. A shoulder of the absorption band at 1020 cm^{-1} can be seen at around 950 cm^{-1}, which is attributed to ν_1 (PO_4^{3-}) vibrational mode. The absorption band at 870 cm^{-1} is assigned to the stretching mode of HPO_4^{2-} groups [38,39]. There was no difference in the positions of absorption bands depending on chemical composition of materials. It can be concluded, that the FTIR spectra confirmed the presence of phosphate ions in the as-prepared samples. All mentioned bands are characteristic of ACP and the broadening demonstrates the absence or very poor crystalline ordering [38], which is in a good agreement with the results obtained by XRD. Moreover, the obtained FTIR spectra did not demonstrate any difference depending on the presence and the nature of incorporated foreign ions. It is also known, that ACP prepared by wet chemical methods can contain trapped carbonate ions [40], which can be identified by the absorption in FTIR spectra at 1490, 1425 and 875 cm^{-1} [41]. In our case, the absorption in these spectral regions is negligible compared to the absorption of phosphate groups, which suggest the presence of a very small amount of carbonates.

The successful introduction of metal ions into ACP matrix was confirmed by means of ICP-OES analysis (Table 1). As seen, the ratios of foreign metal ions and Ca are in good agreement with nominal substitution values for all synthesized samples. In all cases the discrepancies between target and actual molar ratio do not exceed 10%. The ratio of metal ions and phosphorus is slightly lower than target (1.5:1), however the difference is insignificant. To avoid any confusion, all ACP samples will be indicated in the text by a nominal substitution level.

Table 1
Results of elemental analysis of the samples performed by ICP-OES.

ACP samples	$\frac{n(M)\cdot 100\%}{n(Ca+M)}$	$\frac{n(Ca+M)}{n(P)}$
Pristine	–	1.42
5 mol% Mg	4.65	1.42
5 mol% Sr	4.73	1.42
5 mol% Fe	5.20	1.43

The SEM images of pristine and substituted ACPs are given in Fig. 2. It is seen that in all cases powders consist of highly agglomerated particles of nearly spherical shape. Due to the high degree of agglomeration, it is hard to determine the size of the particles precisely. Nevertheless, it is obvious that the size of the most particles lies in the nanoscale range of approximately < 100 nm. At the same time, some larger particles of 200–500 nm also can be seen. There is no visible difference between the powders of different composition, the morphology of all samples is very similar.

Overall, based on the results of XRD, FTIR and SEM analysis it can be concluded that regardless of the partial ion-substitution, the initial powders possess same amorphous structure with the same morphological features. These observations allow to suggest that potential difference in the sorption of radionuclides will be defined by the adsorbents chemical composition.

3.2. ^{85}Sr and ^{60}Co radionuclides adsorption

The adsorption behavior of adsorbents significantly depends on many factors, it is especially important to take into account the pH, nature and concentration of the salt background when adsorbing radionuclides. This is due to the fact that, depending on the pH of the model solutions, the charge of the adsorbent surface (pH_{zpc}) and the state of the metal ions determine the possibility of electrostatic interaction, as well as the course of the dissolution-precipitation processes of calcium phosphates and removed cations. For a comprehensive study of the adsorption characteristics of the obtained adsorbents on the base and metal-substituted calcium phosphates, the influence of the above parameters on the adsorption efficiency of ^{85}Sr and ^{60}Co radionuclides was studied.

3.2.1. Effect of pH

The study of the pH effect was carried out in the range of 4.0–10.0, which allows to evaluate the effectiveness of adsorbents in acidic, neutral and alkaline media (Fig. 3). The presented data show that

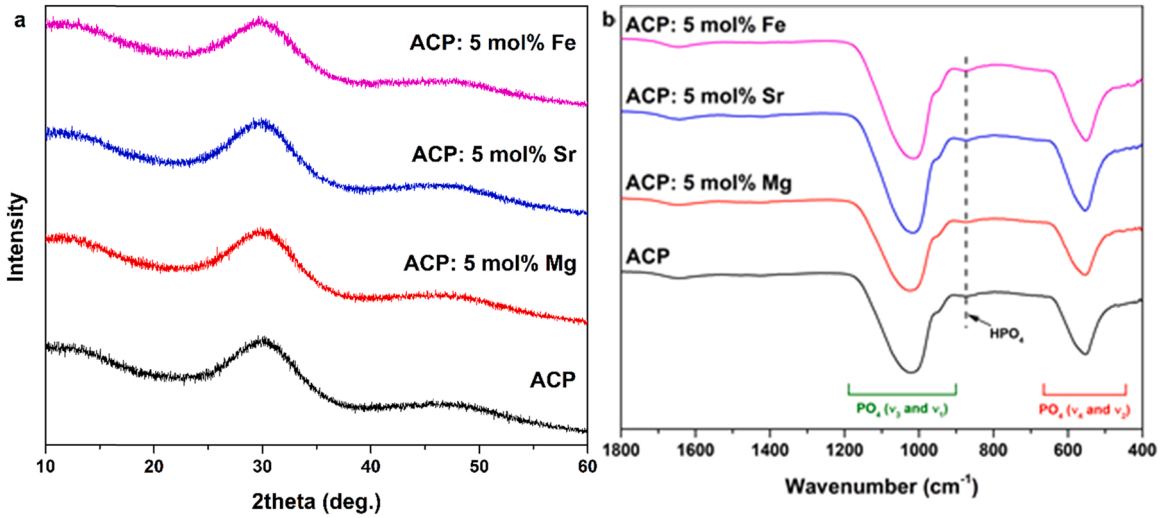

Fig. 1. XRD patterns (a) and FTIR spectra (b) of pristine and ion-substituted ACPs.

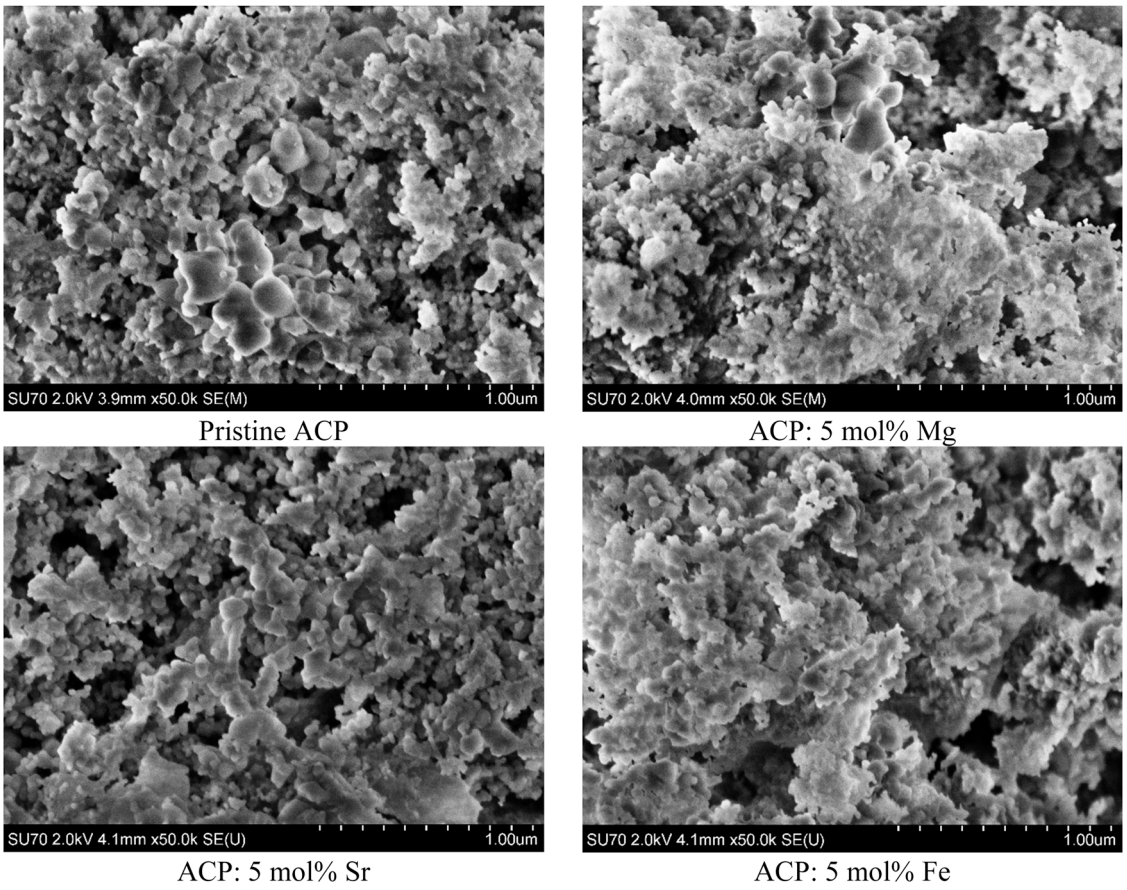

Fig. 2. SEM micrographs (×50 000) of pristine and ion-substituted ACPs.

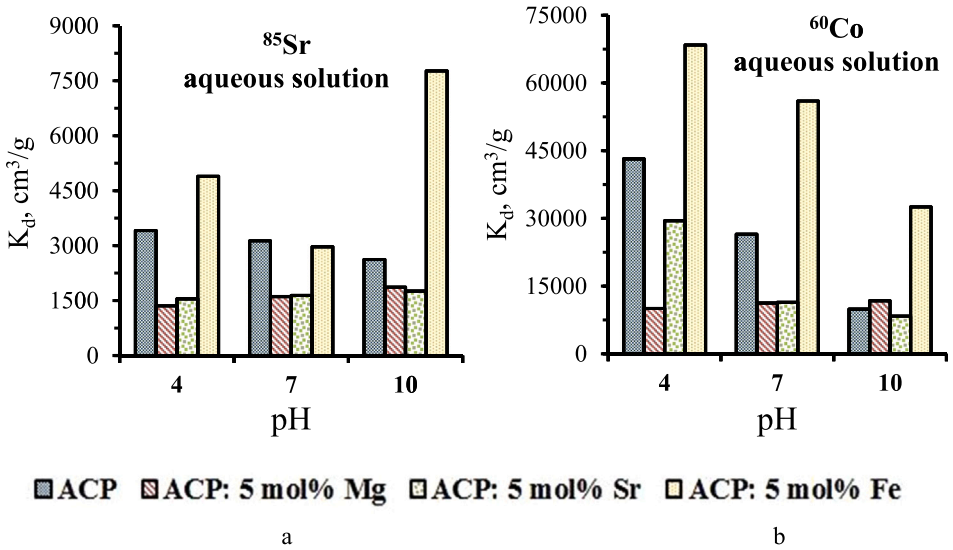

Fig. 3. Effect of pH on K_d (a) ^{85}Sr and (b) ^{60}Co radionuclides in aqueous solutions.

substitution of calcium phosphates with Mg^{2+} and Sr^{2+} does not have a significant effect on the adsorption of ^{85}Sr radionuclides. At the same time, the distribution coefficient of ^{85}Sr with the introduction of Mg^{2+} and Sr^{2+} ions significantly decreases from 3.42×10^3 to $(1.31–1.55)\times 10^3$ cm^3/g, which confirms the negative effect of these cations on the adsorption properties of ACP. The Fe^{3+}-substituted sample showed the highest affinity for ^{85}Sr radionuclides. It should be noted that in an alkaline medium (pH 10.0), the K_d values reached 7.77×10^3 cm^3/g, which is approximately 3-times higher than for the other studied ACPs. The favorable adsorption of ^{85}Sr in an alkaline medium on a Fe^{3+}-substituted sample should be studied additionally. This is in good agreement with the higher adsorption activity of this adsorbent in an acidic medium pH 4.0 (K_d 4.89×10^3 cm^3/g) compared to a neutral pH 7.0 (K_d 2.97×10^3 cm^3/g). This dependency trend of distribution coefficient of ^{85}Sr removal on initial pH is attempted to explore by pH_{zpc} of ACPs (Fig. 4).

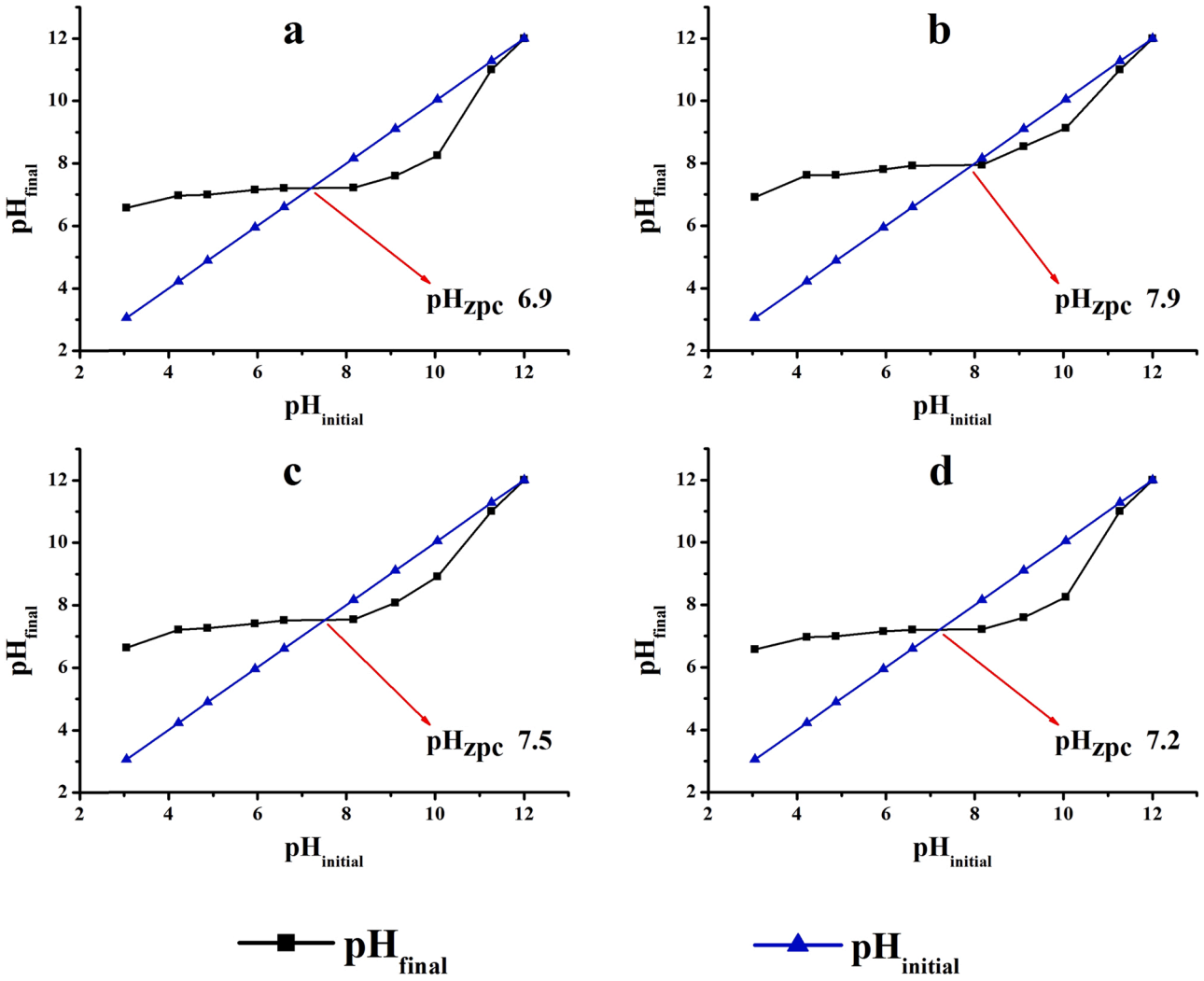

Fig. 4. The pH_{zpc} of (a) initial ACP, (b) ACP: 5 mol% Mg, (c) ACP: 5 mol% Sr, (d) ACP: 5 mol% Fe.

Since the zero point charge (pH_{zpc}) of an adsorbent is that pH of the solution at which the adsorbent is electrically neutral (i.e., the surface of the adsorbent has zero charge), then at $pH_{solution} < pH_{zpc}$ the surface of the adsorbent will have an electropositive nature and vice versa – electronegative at $pH_{solution} > pH_{zpc}$. Thus, the positive Sr^{2+} and Co^{2+} ions should theoretically be well sorbed with an increase in $pH > pH_{zpc}$ to the alkaline region, since the points of zero charge for the obtained initial and metal-substituted ACPs were 6.9, 7.9, 7.5 and 7.2, respectively (Fig. 4). However, according to the analysis of the data on the sorption of ^{85}Sr and ^{60}Co (Fig. 3), such regularity was not observed, which indicates a more complex sorption mechanism.

During the adsorption of ^{60}Co radionuclides, there is a decrease in the removal efficiency of these cations with an increase in pH. As with the adsorption of ^{85}Sr radionuclides, Fe^{3+}-substituted and pristine ACP have the highest affinity to ^{60}Co for which K_d reached 6.84×10^4 and 4.32×10^4 cm^3/g in an acidic medium (pH 4.0) and 6.84×10^4 and 4.32×10^4 cm^3/g in an alkaline medium (pH 10.0), respectively. It is known that at low pH values < 4.0, Co^{2+} ions predominate in the aqueous solutions, and at pH 10.0, the formation of polynuclear hydroxocomplexes and colloidal cobalt hydroxide occurs. These features of the presence of Co^{2+} ions in solution at different pH cause differences in the adsorption behavior of ACP adsorbents to ^{85}Sr and ^{60}Co radionuclides.

3.2.2. Selectivity in 0.1 M NaCl solutions

Interesting results were obtained when studying the selectivity of ACPs with the background of 0.1 M NaCl solutions (Fig. 5). Thus, regardless of the composition of the adsorbents, a decrease in K_d ^{85}Sr was observed compared to aqueous solutions. At the same time, for all ion-substituted ACPs, the K_d values were significantly lower than for pristine ACP. In contrast to aqueous solutions, an increase in pH from 4.0 to 10.0 is accompanied by an increase in K_d ^{85}Sr and for the most selective adsorbent of the pristine ACP was $(1.29–1.67) \times 10^3$ cm^3/g.

The adsorption behavior of ACPs to ^{60}Co radionuclides in 0.1 M NaCl solutions (Fig. 5) has a similar character as in an aqueous solution (Fig. 3). At the same time, all adsorbents showed superior K_d values exceeding 10^4 cm^3/g. Also, Fe^{3+}-substituted and pristine ACP have 2–2.5 times higher affinity to ^{60}Co compared to Mg^{2+}- and Sr^{2+}-substituted samples. Therefore, the increase of pH negatively effects on the adsorption efficiency of ^{60}Co radionuclides in 0.1 M NaCl solutions, which is associated with changes in the state of Co^{2+} ions at different pH.

3.2.3. Selectivity in 0.01 M $CaCl_2$ solutions

The dramatic decrease of K_d ^{85}Sr in 0.01 M $CaCl_2$ solutions was observed for ACP adsorbents (Fig. 6a). In addition, the most effective Fe^{3+}-substituted sample practically lost its adsorption activity in the entire studied pH range (K_d < 140 cm^3/g). This indicates a high competitive adsorption of Ca^{2+} ions, which are characterized by similar chemical properties with Sr^{2+} ions. It should be taken into account that

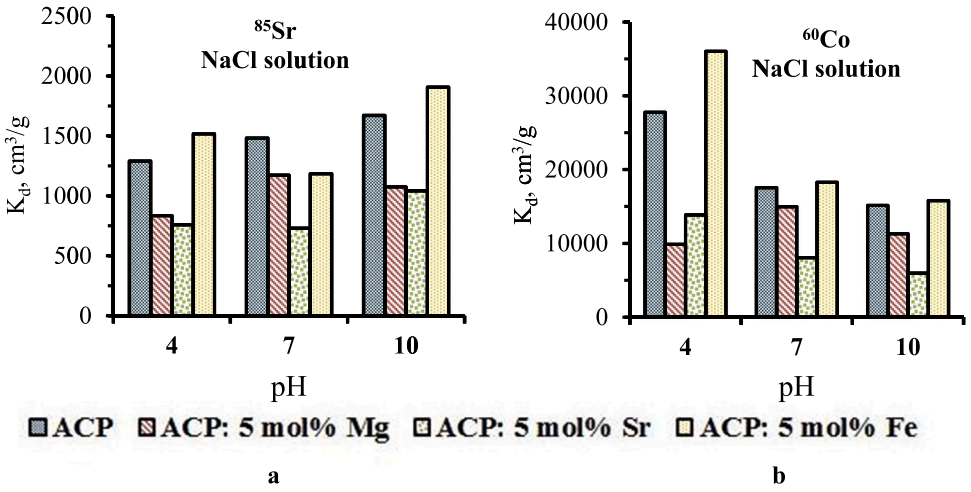

Fig. 5. Effect of pH on K_d (a) ^{85}Sr and (b) ^{60}Co radionuclides in 0.1 M NaCl solutions.

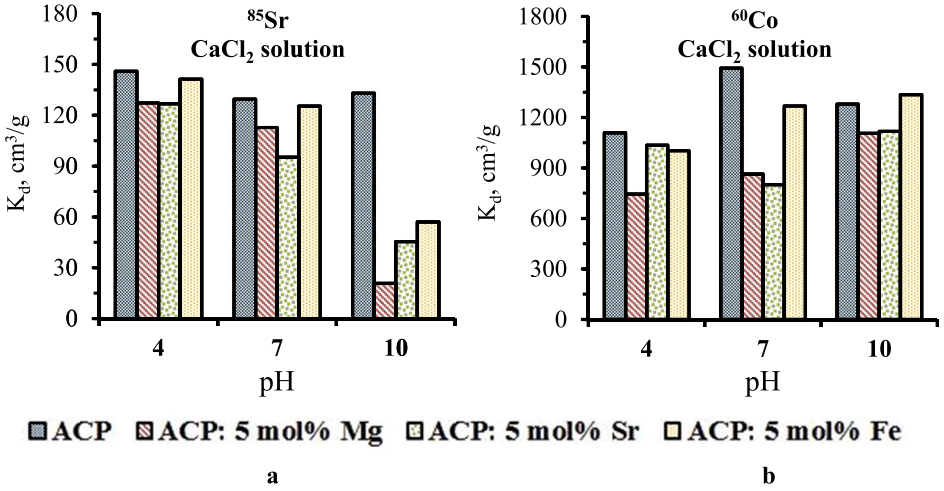

Fig. 6. Effect of pH on K_d (a) ^{85}Sr and (b) ^{60}Co radionuclides in 0.01 M $CaCl_2$ solutions.

the concentration of ^{85}Sr radionuclides in model solutions does not exceed 10^{-9} M, which is incomparably lower than the concentration of Ca^{2+} ions.

The expected decrease in adsorption properties of ACP samples was shown for ^{60}Co radionuclides (Fig. 6b). Therefore, the K_d values reached (1.11–1.49)× 10^3 cm^3/g, which is acceptable for their application. It is important that in the case of ^{60}Co radionuclides in 0.01 M $CaCl_2$ solutions, the pH did not significantly affect the effectiveness of the

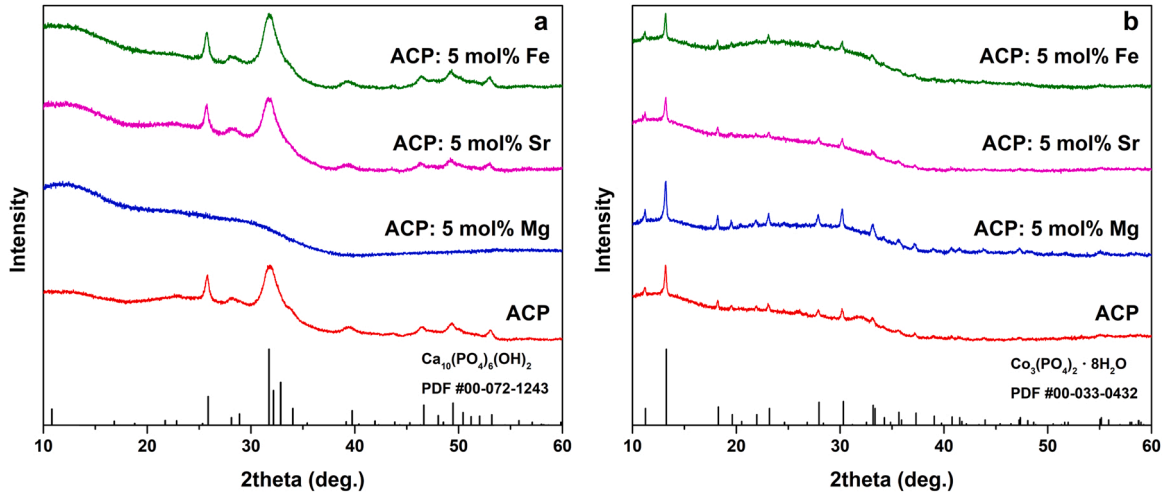

Fig. 7. XRD patterns of ACPs after (a) Sr^{2+} and (b) Co^{2+} ions adsorption.

adsorbents. However, it was previously shown that during adsorption from aqueous and 0.1 M NaCl solutions, there was a pronounced decrease in K_d.

3.3. Adsorption mechanism

For the understanding of adsorption mechanism of radionuclides, for safety reason ACP adsorbents were saturated by stable Sr^{2+} and Co^{2+} ions from 2.0 g/L $Sr(NO_3)_2$ and $Co(NO_3)_2$ solutions for further XRD, FTIR, SEM, and EDX analysis. The XRD patterns of the ACPs after the adsorption experiment are represented in Fig. 7. It is seen that during the adsorption process the phase transformation of ACP occurred, which obviously depends both on the nature of substituent ion and radionuclide. In the case of Sr^{2+} adsorption (Fig. 7a) the phase conversion from ACP to calcium HAp was confirmed for all adsorbents except of Mg^{2+}-substituted ACP. The positions of the reflection peaks are in good agreement with the standard XRD data for hexagonal calcium HAp (PDF #00-072-1243). Broadening of the diffraction peaks indicates that obtained powders possess low degree of crystallinity. It is well known, that in aqueous medium ACP crystallizes to HAp, however, the presence of foreign ions can retard the crystallization process [42].

Smaller divalent cations, particularly Mg^{2+}, inhibit the formation of crystalline HAp and may lead to the formation of low-crystalline material or completely prevent phase transformation to HAp [42–44]. These phenomena explain the amorphous nature of Mg^{2+}-substituted ACP after the adsorption procedure, as ionic radius of Mg^{2+} ions are significantly lower than that of Ca^{2+} [45]. It can be concluded that the dissolution-precipitation adsorption mechanism is predominate for Sr^{2+} ions. In that case, the regularities of ^{85}Sr radionuclides adsorption in $CaCl_2$ solution could be clarify, due to suppresses the solubility of ACP.

Definitely different pattern was observed after Co^{2+} ions adsorption (Fig. 7b). Small amount of HAp as a secondary crystal phase was observed only in the adsorbent consisted of pristine ACP. Regardless of the chemical composition of initial powders, all XRD patterns are dominated by the reflections raised from monoclinic $Co_3(PO_4)_2{\cdot}8H_2O$ (PDF #00-033-0432). Possible explanation is also related to the ionic radius of Co^{2+} ions and its inhibitory effect on the formation of HAp. Co^{2+} ions are significantly smaller compared to Ca^{2+} [45], therefore, high Co^{2+} concentration in the model solution prevents the crystallization of HAp. At the same time, relatively soluble ACP released the phosphate ions into solution, which further precipitated in the form of more stable $Co_3(PO_4)_2{\cdot}8H_2O$. So, the chemisorption mechanism is clear supported by XRD analysis of spent adsorbents. The presented results are in a good agreement with the data of ^{60}Co radionuclide adsorption (Section 3.2).

The FTIR spectra of the ACPs after the adsorption experiment are depicted in Fig. 8. It is obvious that after the contact with Sr^{2+} model solution (Fig. 8a) the shape of the spectra changed considerably, compared to that of initial ACPs (Fig. 2) with an exception for the spectrum of Mg-substituted ACP, which does not differ from the spectrum of initial powders. For the other spectra the sharper and well split absorption bands go hand in hand with the transformation of amorphous materials to crystalline. The obtained spectra are typical of calcium HAp and confirm the XRD data [43]. The absorption bands centered at 1090, 1025 (υ_3) and 960 cm^{-1} (υ_1) correspond to the P–O stretching vibration mode and the bands located at 600 and 560 cm^{-1} (υ_4) are assigned to O–P–O bending mode of the phosphate group. The weak band at 471 cm^{-1} (υ_2) is attributed to phosphate bending mode [46]. Finally, the absorption band located at around 868 cm^{-1} is attributed to P–O(H) stretching mode of the HPO_4^{2-} group, which can be assumed as an evidence of the formation of calcium-deficient HAp (CDHA, $Ca_{10-x}(PO_4)_{6-x}(HPO_4)_x(OH)_{2-x}$). Contrary to the stoichiometric calcium HAp, which does not contain HPO_4^{2-} group, it can been found in the crystal structure of CDHA.

The FTIR spectra of ACPs, contacted with Co^{2+} model solution, are depicted in Fig. 8b. It is seen, that spectra remained very similar to those of initial powders. Despite the formation of crystalline $Co_3(PO_4)_2{\cdot}8H_2O$, there were no additional absorption bands in the FTIR spectra. These data suggest that ACP is still present in these samples in significant amount, which cannot be detected by XRD. On the other hand, the overlapping of the absorption bands in FTIR spectra does not allow to observe $Co_3(PO_4)_2{\cdot}8H_2O$ by vibrational spectroscopy.

SEM microscopy was further employed to investigate the morphological changes in ACPs after the adsorption and to check the coexistence of two phases in ACPs contacted with Co^{2+} model solution. The SEM images of powders after Sr^{2+} ions adsorption are shown in Fig. 9. A very clear correlation can be seen, the morphology of all samples converted to CDHA (ACP, Sr^{2+}-substituted ACP and Fe^{3+}-substituted ACPs) changed considerably compared to that of initial materials. It is known that HAp formed in the result of hydrolysis reaction tends to form flake-like particles [9]. In our case we observed very fine flakes stacked to each other. On the other hand, Mg^{2+}-substituted ACP did not change its morphology, which agrees with the absence of structural transformations in this material.

Fig. 10 demonstrates the SEM images of ACPs after the sorption of Co^{2+} ions. These images confirm very well the biphasic nature of powders, which was predicted based on XRD and FTIR analysis. The presence of particles of a very different morphology is evident. While the

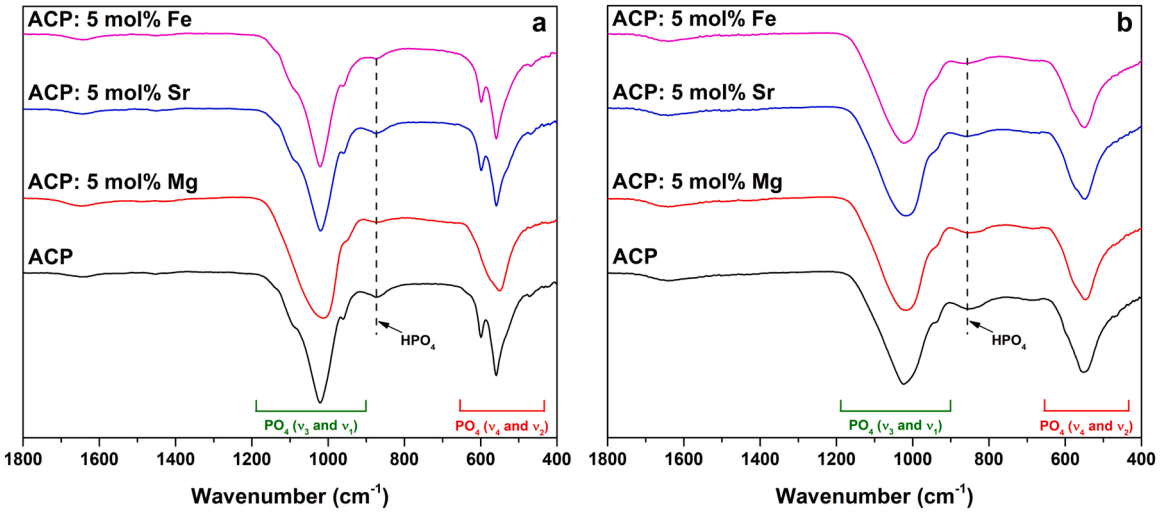

Fig. 8. FTIR spectra of ACPs after (a) Sr^{2+} and (b) Co^{2+} ions adsorption.

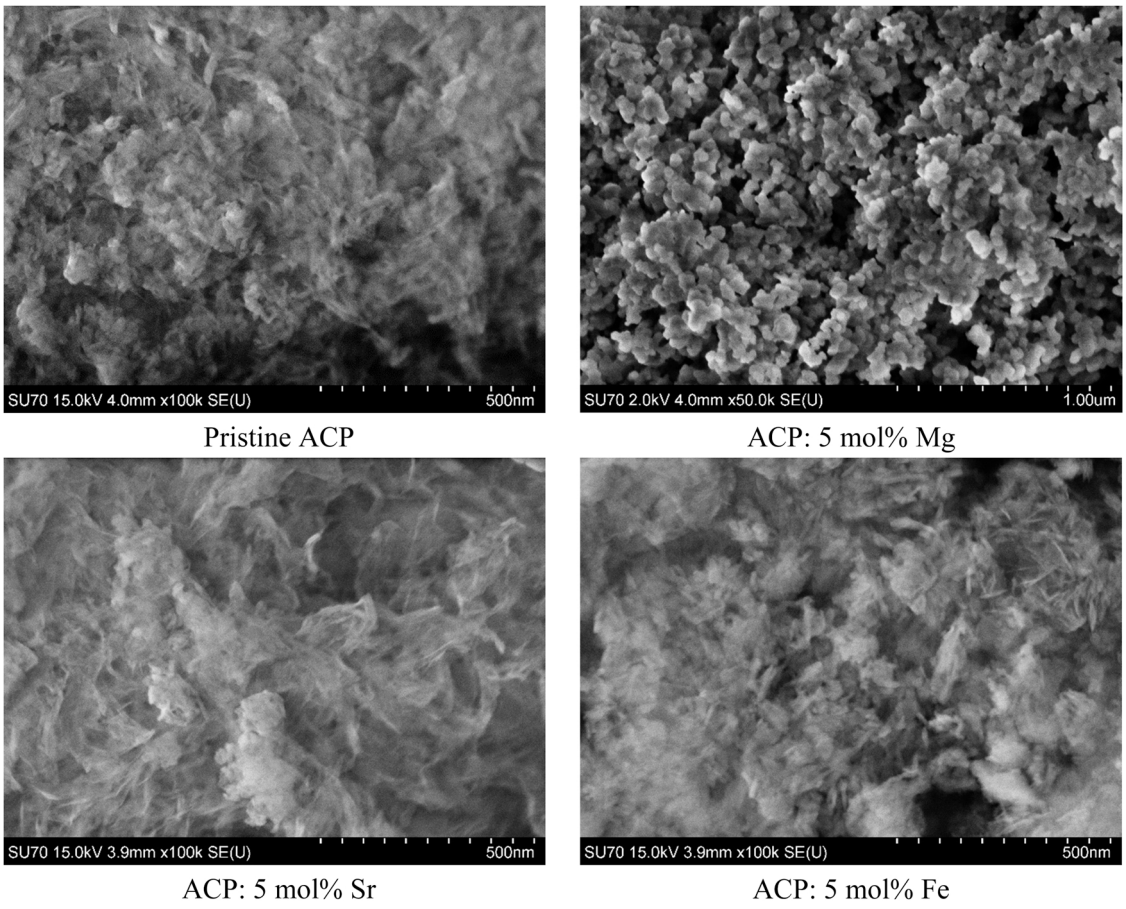

Fig. 9. SEM micrographs of ACPs after Sr^{2+} ions adsorption (×100 000).

large particles with layered structure can be assigned to $Co_3(PO_4)_2 \cdot 8H_2O$, the small spherical particles correspond to ACP. There was no visible difference between the powder morphology depending on the chemical composition of initial ACPs. Overall, it can be summarized, that the results of SEM analysis are in good agreement with the results obtained by XRD and FTIR and the chemisorption mechanism is supported for ^{60}Co radionuclide adsorption.

The elemental composition of adsorbents saturated with Sr^{2+} and Co^{2+} ions is shown in Table 2. In the adsorption process, the content of Mg, Sr, Fe atoms in metal-substituted ACPs was practically not changed. This confirms the stability of adsorbents structure in the process of model aqueous solutions purification. The content of Sr atoms in the samples was in good agreement with the data on the distribution coefficients K_d of ^{85}Sr and ^{60}Co radionuclides. ACP samples after adsorption of Co^{2+} ions had 2-times higher content of Co atoms than in the case of samples after Sr^{2+} ions adsorption. This is due to the different mechanism of adsorption of the studied ions, and as a consequence, different affinity. At the same time, the Fe-substituted sample was characterized by the highest content of Co and Sr atoms among all studied adsorbents. Thus, the EDX analysis data is in good agreement with the results of XRD, FT-IR and the adsorption of ^{85}Sr and ^{60}Co radionuclides.

3.4. Comparison with others adsorbents

A comparative study of distribution coefficient (K_d) of ACPs and other widely used world analogs of adsorbents was shown in Table 3. Fe-substituted ACPs demonstrated the superior adsorption efficiency towards ^{85}Sr (Log (K_d) 3.89) and ^{60}Co (Log (K_d) 4.84) radionuclides from aqueous solutions and can be efficiently used for the waste water treatment in nuclear industry. It should be noted that obtained adsorbents had a high affinity for strontium and cobalt radionuclides, which is especially important for single-stage purification of liquid radioactive waste of complex radionuclide composition. The real LRW has complex composition and besides Na^+ and Ca^{2+} metal ions contains complexonate agents (EDTA, HEPD), surfactants, and other chemicals. It could be affected on the adsorbents efficiency. The influencing of LRW chemical composition on ACP adsorbents efficiency will be performed in further studies.

The further disposal of high activity radioactive waste is an urgent task. This study did not aim to develop the technology of radionuclides immobilization. Meanwhile, the common way for spent adsorbents management it is their cementation or formation of ceramic matrices. Especially, it is well-known that phosphates with the apatite (britholite) structure is prospect materials for various radionuclides immobilization [54]. It should be studied additionally.

4. Conclusions

Mg^{2+}-, Sr^{2+}-, and Fe^{3+}-substituted amorphous calcium phosphates as a high efficient ^{85}Sr and ^{60}Co radionuclides adsorbents were prepared by a simple precipitation method. The effect of synthesis conditions on phase and chemical composition, morphology, and adsorption characteristics was studied. The obtained materials were amorphous calcium phosphates that is supported by XRD and FTIR analysis. Effect of pH, NaCl, $CaCl_2$ salt backgrounds on K_d (^{85}Sr, ^{60}Co) were studied. The most efficient Fe^{3+}-substituted calcium phosphate adsorbent had a superior distribution coefficient to ^{85}Sr (K_d 7.77 $\times 10^3$ cm^3/g) and ^{60}Co (K_d 6.84 $\times 10^4$ cm^3/g) radionuclides at pH of 10.0 and 4.0, respectively. The high selectivity of obtained adsorbents to ^{85}Sr and ^{60}Co radionuclides

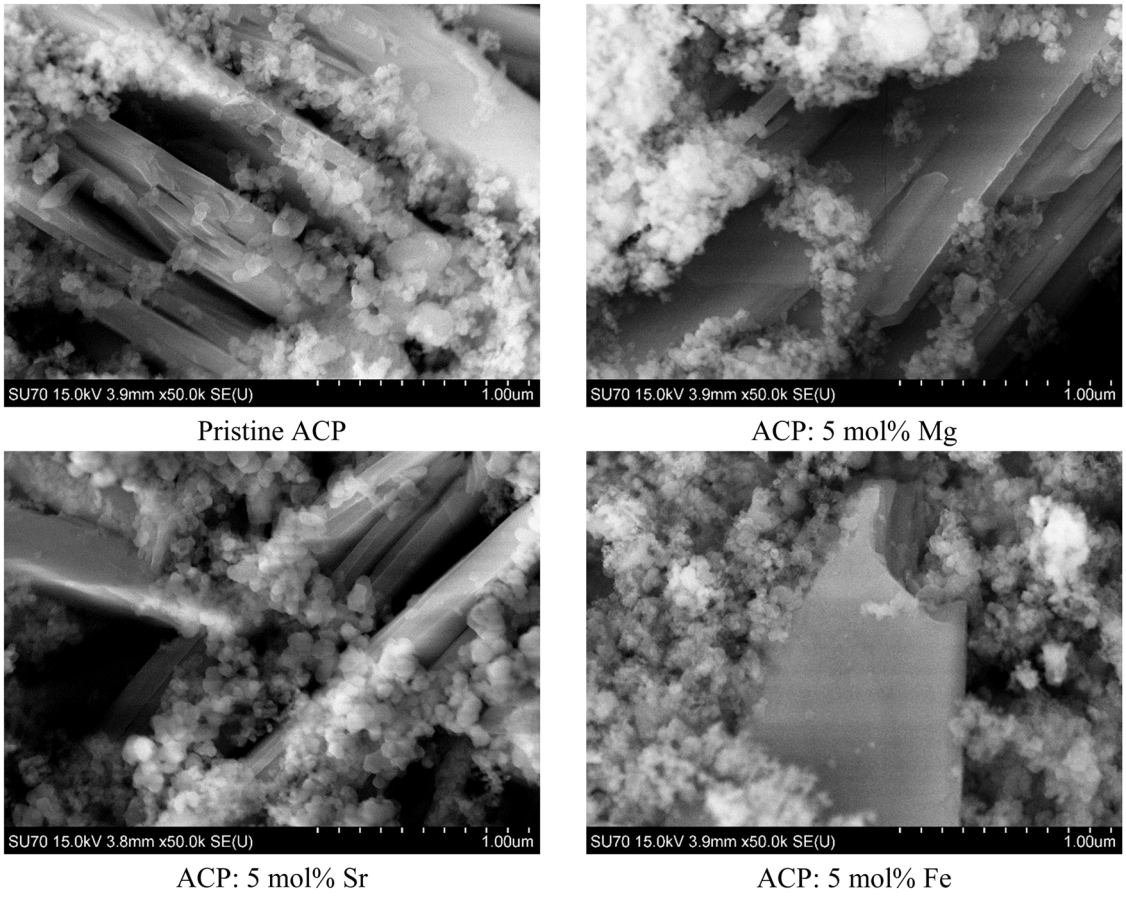

Fig. 10. SEM micrographs (×50 000) of ACPs after Co^{2+} ions adsorption.

Table 2
Composition of ACPs after Sr^{2+} and Co^{2+} ions adsorption according to EDX analysis.

ACP samples	Content of element, at%[a]						
	O	P	Ca	Mg	Sr	Fe	Co
	Sr^{2+} ions adsorption						
Pristine	59.94	9.74	12.17	–	0.86	–	–
5 mol% Mg	64.47	9.50	10.75	0.573	0.77	–	–
5 mol% Sr	60.33	10.05	11.65	–	1.75	–	–
5 mol% Fe	54.57	9.92	11.77	–	2.10	0.89	–
	Co^{2+} ions adsorption						
Pristine	64.38	9.27	9.65	–	–	–	1.51
5 mol% Mg	64.17	8.21	8.78	0.42	–	–	1.31
5 mol% Sr	61.93	9.34	10.18	–	0.72	–	1.35
5 mol% Fe	60.18	9.66	13.51	–	–	0.94	1.98

[a] The signals of holder (carbon, aluminum) were not presented.

Table 3
Comparison obtained ACP samples with various adsorbents (K_d in cm^3/g).

Adsorbent	Log (K_d) cm^3/g		Reference
	$^{85,\ 90}Sr$	^{60}Co	
Nanotube titanates	6.00	–	[47]
Hexagonal Tungsten Bronzes	3.36–4.00	–	[48]
KMS-2	5.17	–	[49]
Graphene oxide@HAp	3.90	–	[50]
AMP-PAN	2.61	–	[51]
Nanotubes TiO_2	–	3.49	[52]
Ti-Ca-Mg phosphates	4.49	4.91	[53]
ACP (5 mol% Fe)	3.89	4.84	This work

showed at 0.1 M NaCl background, when K_d sharply decreased in presence of 0.01 M $CaCl_2$ solution. The dissolution-precipitation and chemisorption mechanism for ^{85}Sr and ^{60}Co radionuclides adsorption was defined. Fe^{3+}-substituted calcium phosphate showed the comparable adsorption efficiency to ^{85}Sr and ^{60}Co radionuclides with widely used adsorbents, which is suitable for single-stage purification of liquid radioactive waste.

CRediT authorship contribution statement

Andrei Ivanets: Conceptualization, Methodology, Writing – original draft. **Aleksej Zarkov**: Adsorbents synthesis and characterization, Writing – review & results discussion. **Vladimir Prozorovich**: Investigation, Visualization, Data curation, Formal analysis. **Katsiaryna Venhlinskaya**: Performance of radionuclides adsorption experiment. **Artsiom Radkevich**: Performance of radionuclides adsorption experiment, Editing. **Jen-Chang Yang**: SEM-EDX analysis, Editing. **Evgeniy Papynov**: Revision manuscript, Editing. **Sofiya Yarusova**: Revision manuscript, Editing. **Aivaras Kareiva**: Project administration, Funding acquisition, Editing.

Declaration of Competing Interest

The authors declare that they have no known competing financial interests or personal relationships that could have appeared to influence the work reported in this paper.

Acknowledgements

The study was financially supported by National Academy of Sciences of Belarus (grant #2.1.02). This project has received funding from

European Social Fund (project No 09.3.3-LMT-K-712-19-0069) under grant agreement with the Research Council of Lithuania (LMTLT). Andrius Pakalniskis (Vilnius University) is highly acknowledged for technical assistance.

References

[1] M. Du, J. Chen, K. Liu, H. Xing, C. Song, Recent advances in biomedical engineering of nano-hydroxyapatite including dentistry, cancer treatment and bone repair, Composites Part B 215 (2021), 108790, https://doi.org/10.1016/j.compositesb.2021.108790.

[2] G. Wei, C. Gong, K. Hu, Ya Wang, Ya Zhang, Biomimetic hydroxyapatite on graphene supports for biomedical applications: a review, Nanomaterials 9 (10) (2019) 1435, https://doi.org/10.3390/nano9101435.

[3] A. Sobczak-Kupiec, A. Drabczyk, W. Florkiewicz, M. Głąb, S. Kudłacik-Kramarczyk, S.łota Dagmara, A. Tomala, B. Tyliszczak, Review of the applications of biomedical compositions containing hydroxyapatite and collagen modified by bioactive components, Materials 14 (9) (2021) 2096, https://doi.org/10.3390/ma14092096.

[4] S. Mondal, U. Pal, 3D hydroxyapatite scaffold for bone regeneration and local drug delivery applications, J. Drug Deliv. Sci. Technol. 53 (2019), 101131, https://doi.org/10.1016/j.jddst.2019.101131.

[5] Th Varadavenkatesan, R. Vinayagam, Sh Pai, K. Brindhadevi, A. Pugazhendhi, R. Selvaraj, Synthesis, biological and environmental applications of hydroxyapatite and its composites with organic and inorganic coatings, Prog. Org. Coat. 151 (2021), 106056, https://doi.org/10.1016/j.porgcoat.2020.106056.

[6] H. Bensalah, S.A. Saad AlamiYounssi, M. Ouammou, A. Gurlo, M.F. Bekheet, Azo dye adsorption on an industrial waste-transformed hydroxyapatite adsorbent: kinetics, isotherms, mechanism and regeneration studies, J. Environ. Chem. Eng. 8 (3) (2020), 103807, https://doi.org/10.1016/j.jece.2020.103807.

[7] A. Nayak, B. Bhushan, Hydroxyapatite as an advanced adsorbent for removal of heavy metal ions from water: focus on its applications and limitations, Mater. Today Proc. 46 (20) (2021) 11029–11034, https://doi.org/10.1016/j.matpr.2021.02.149.

[8] X. Zou, Ya Zhao, Zh Zhang, Preparation of hydroxyapatite nanostructures with different morphologies and adsorption behavior on seven heavy metals ions, J. Contam. Hydrol. 226 (2019), 103538, https://doi.org/10.1016/j.jconhyd.2019.103538.

[9] M.J. Rigali, P.V. Brady, R.C. Moore, Radionuclide removal by apatite, Am. Miner. 101 (2016) 2611–2619, https://doi.org/10.2138/am-2016-5769.

[10] A.I. Ivanets, N.V. Kitikova, I.L. Shashkova, M.Yu Roshchina, V. Srivastava, M. Sillanpää, Adsorption performance of hydroxyapatite with different crystalline and porous structure towards metal ions in multicomponent solution, J. Water Process Eng. 32 (2019), 100963, https://doi.org/10.1016/j.jwpe.2019.100963.

[11] C. Stötzel, F.A. Müller, F. Reinert, F. Niederdraenk, J.E. Barralet, U. Gbureck, Ion adsorption behaviour of hydroxyapatite with different crystallinities, Colloids Surf. B 74 (1) (2009) 91–95, https://doi.org/10.1016/j.colsurfb.2009.06.031.

[12] H. Bensalah, M.F. Bekheet, S.A. Younssi, M. Ouammou, A. Gurlo, Hydrothermal synthesis of nanocrystalline hydroxyapatite from phosphogypsum waste, J. Environ. Chem. Eng. 6 (1) (2018) 1347–1352, https://doi.org/10.1016/j.jece.2018.01.052.

[13] J. Indira, K.S. Malathi, Comparison of template mediated ultrasonic and microwave irradiation method on the synthesis of hydroxyapatite nanoparticles for biomedical applications, Mater. Today Proc. (2021), https://doi.org/10.1016/j.matpr.2021.03.028.

[14] K. He, G.-Yo Xiao, W.-H. Xu, R.-F. Zhu, Yu-P. Lu, Ultrasonic enhancing amorphization during synthesis of calcium phosphate, Ultrason. Sonochem. 21 (2) (2014) 499–504, https://doi.org/10.1016/j.ultsonch.2013.08.011.

[15] M.E. Jaramillo, C.P.O. Orozco, Multiphase calcium phosphate nanorods produced by microwave-assisted molten salt synthesis: particle size RSM optimization, Ceram. Int. 47 (12) (2021) 17202–17209, https://doi.org/10.1016/j.ceramint.2021.03.031.

[16] V. Uskoković, Ion-doped hydroxyapatite: an impasse or the road to follow? Ceram. Int. 46 (8B) (2020) 11443–11465, https://doi.org/10.1016/j.ceramint.2020.02.001.

[17] H. Ding, H. Pan, X. Xu, R. Tang, Toward a detailed understanding of magnesium ions on hydroxyapatite crystallization inhibition, 2014, Cryst. Growth Des. 14 (2) (2014) 763–769, https://doi.org/10.1021/cg401619s.

[18] N.V. Kitikova, A.I. Ivanets, I.L. Shashkova, Synthesis of hydroxyapatite in the presence of hydroxyethylidenediphosphonic acid and Mg^{2+} ions as crystallization inhibitors, Inorg. Mater. 56 (2020) 47–55, https://doi.org/10.1134/S0020168520010057.

[19] G. Kazakova, T. Safronova, D. Golubchikov, O. Shevtsova, J.V. Rau, Resorbable Mg^{2+}-containing phosphates for bone tissue repair, Materials 14 (2021) 4857, https://doi.org/10.3390/ma14174857.

[20] M. Kalbarczyk, A. Szcześ, D. Sternik, The preparation of calcium phosphate adsorbent from natural calcium resource and its application for copper ion removal, Environ. Sci. Pollut. Res. 28 (2020) 1725–1733, https://doi.org/10.1007/s11356-020-10585-7.

[21] A.I. Ivanets, V. Srivastava, N.V. Kitikova, I.L. Shashkova, M. Sillanpää, Non-apatite Ca-Mg phosphate sorbent for removal of toxic metal ions from aqueous solutions, J. Environ. Chem. Eng. 5 (2) (2017) 2010–2017, https://doi.org/10.1016/j.jece.2017.03.041.

[22] Sh Yu, H. Mei, X. Chen, X. Tan, B. Ahmad, A. Alsaedi, T. Hayat, X. Wang, Impact of environmental conditions on the sorption behavior of radionuclide ^{90}Sr(II) on Na-montmorillonite, J. Mol. Liq. 203 (2015) 39–46, https://doi.org/10.1016/j.molliq.2014.12.041.

[23] Agency for Toxic Substances and Disease Registry (ATSDR), Toxicological profile for Strontium. Atlanta, GA: U.S. Department of Health and Human Services, Public Health Service, 2004. ⟨https://wwwn.cdc.gov/TSP/ToxProfiles/ToxProfiles.aspx?id=656&tid=120⟩.

[24] M.P. Đorđević, J. Maletaškić, N. Stanković, B. Babić, K. Yoshida, T. Yano, B. Matović, In-situ immobilization of Sr radioactive isotope using nanocrystalline hydroxyapatite, Ceram. Int. 44 (2) (2018) 1771–1777, https://doi.org/10.1016/j.ceramint.2017.10.110.

[25] B. Matovic, M.P. Djordjevic, J. Maletaskic, K. Yoshida, T. Yano, Preparation and properties of hydroxyapatite nano-spheres for immobilization of Sr isotopes, Energy Procedia 131 (2017) 140–145, https://doi.org/10.1016/j.egypro.2017.09.419.

[26] M. Vučinić-Vasić, B. Antić, M. Bošković, A. Antić, J. Blanuša, Hydroxyapatite/iron oxide nanocomposite prepared by high energy ball milling, Process Appl. Ceram. 13 (2) (2019) 210–217, https://doi.org/10.2298/PAC1902210V.

[27] M. Ajeesh, B.F. Francis, J. Annie, P.R. Harikrishna Varma, Nano iron oxide-hydroxyapatite composite ceramics with enhanced radiopacity, J. Mater. Sci. Mater. Med. 21 (2010) 1427–1434, https://doi.org/10.1007/s10856-010-4005-9.

[28] M. Sneha, N.M. Sundaram, Preparation and characterization of an iron oxide-hydroxyapatite nanocomposite for potential bone cancer therapy, Int. J. Nanomed. 10 (1) (2015) 99–106, https://doi.org/10.2147/IJN.S79985.

[29] L. Gu, X. He, Zh Wu, Mesoporous Fe_3O_4/hydroxyapatite composite for targeted drug delivery, Mater. Res. Bull. 59 (2014) 65–68, https://doi.org/10.1016/j.materresbull.2014.06.018.

[30] L. Cui, L. Hu, X. Guo, Ya Zhang, Ya Wang, Q. Wei, B. Du, Kinetic, isotherm and thermodynamic investigations of Cu2 + adsorption onto magnesium hydroxyapatite/ferroferric oxide nano-composites with easy magnetic separation assistance, J. Mol. Liq. 198 (2014) 157–163, https://doi.org/10.1016/j.molliq.2014.06.016.

[31] A. Vahdat, B. Ghasemi, M. Yousefpour, Mechanical properties of the hydroxyapatite and magnetic nanocomposite of hydroxyapatite adsorbents, S. Afr. J. Chem. Eng. 33 (2020) 90–94, https://doi.org/10.1016/j.sajce.2020.05.007.

[32] G.C. Ispas, R. Manea, R.I. Brazdis, A.M. Baroi, T. Fistos, R.C. Fierascu, M.F. Raduly, Iron oxide/phosphatic materials composites with potential applications in environmental protection, Materials 13 (21) (2020) 5034, https://doi.org/10.3390/ma13215034.

[33] S. Pai, S. M Kini, R. Selvaraj, A. Pugazhendhi, A review on the synthesis of hydroxyapatite, its composites and adsorptive removal of pollutants from wastewater, J. Water Process Eng. 38 (2020), 101574, https://doi.org/10.1016/j.jwpe.2020.101574.

[34] L. Sinusaite, A. Kareiva, A. Zarkov, Thermally induced crystallization and phase evolution of amorphous calcium phosphate substituted with divalent cations having different sizes, Cryst. Growth Des. 21 (2) (2021) 1242–1248, https://doi.org/10.1021/acs.cgd.0c01534.

[35] D. Griesiute, L. Sinusaite, A. Kizalaite, A. Antuzevics, K. Mazeika, D. Baltrunas, T. Goto, T. Sekino, A. Kareiva, A. Zarkov, The influence of Fe^{3+} doping on thermally induced crystallization and phase evolution of amorphous calcium phosphate, CrystEngComm 23 (26) (2021) 4627–4637, https://doi.org/10.1039/D1CE00371B.

[36] I. Shashkova, N. Kitikova, A. Ivanets, Features of the behavior of calcium and magnesium phosphate sorbents in water and electrolyte solutions, Russ. J. Appl. Chem. 94 (5) (2021) 601–615, https://doi.org/10.1134/S1070427221050086.

[37] J. Vecstaudza, M. Gasik, J. Locs, Amorphous calcium phosphate materials: formation, structure and thermal behaviour, J. Eur. Ceram. Soc. 39 (4) (2019) 1642–1649, https://doi.org/10.1016/j.jeurceramsoc.2018.11.003.

[38] C. Combes, C. Rey, Amorphous calcium phosphates: synthesis, properties and uses in biomaterials, Acta Biomater. 6 (9) (2010) 3362–3378, https://doi.org/10.1016/j.actbio.2010.02.017.

[39] C.J.S. Ibsen, D. Chernyshov, H. Birkedal, Apatite formation from amorphous calcium phosphate and mixed amorphous calcium phosphate/amorphous calcium carbonate, Chem. Eur. J. 22 (35) (2016) 12347–12357, https://doi.org/10.1002/chem.201601280.

[40] S. Somrani, C. Rey, M. Jemal, Thermal evolution of amorphous tricalcium phosphate, J. Mater. Chem. 13 (4) (2003) 888–892, https://doi.org/10.1039/B210900J.

[41] Y. Li, F. Kong, W. Weng, Preparation and characterization of novel biphasic calcium phosphate powders (α-TCP/HA) derived from carbonated amorphous calcium phosphates, J. Biomed. Mater. Res. B Appl. Biomater. 89B (2) (2009) 508–517, https://doi.org/10.1002/jbm.b.31242.

[42] S.V. Dorozhkin, Amorphous calcium (ortho)phosphates, Acta Biomater. 6 (12) (2010) 4457–4475, https://doi.org/10.1016/j.actbio.2010.06.031.

[43] L. Sinusaite, A. Popov, E. Raudonyte-Svirbutaviciene, J.-C. Yang, A. Kareiva, A. Zarkov, Effect of Mn doping on hydrolysis of low-temperature synthesized metastable alpha-tricalcium phosphate, Ceram. Int. 47 (9) (2021) 12078–12083, https://doi.org/10.1016/j.ceramint.2021.01.052.

[44] H. Ding, H. Pan, X. Xu, R. Tang, Toward a detailed understanding of magnesium ions on hydroxyapatite crystallization inhibition, Cryst. Growth Des. 14 (2) (2014) 763–769, https://doi.org/10.1021/cg401619s.

[45] R.D. Shannon, Revised effective ionic radii and systematic studies of interatomic distances in halides and chalcogenides, Acta Crystallogr. A 32 (5) (1976) 751–767.

[46] S. Koutsopoulos, Synthesis and characterization of hydroxyapatite crystals: a review study on the analytical methods, J. Biomed. Mater. Res. 62 (4) (2002) 600–612, https://doi.org/10.1002/jbm.10280.

[47] S. Kasap, S. Piskin, H. Tel, Titanate nanotubes: preparation, characterization and application in adsorption of strontium ion from aqueous solution, Radiochim. Acta 100 (2012) 925–929, https://doi.org/10.1524/ract.2012.1981.
[48] C.S. Griffith, V. Luca, J.V. Hanna, K.J. Pike, M.E. Smith, G.S. Thorogood, Microcrystalline hexagonal tungsten bronze. 1. Basis of ion exchange selectivity for cesium and strontium, Inorg. Chem. 48 (2009) 5648–5662, https://doi.org/10.1021/ic801294x.
[49] M.J. Manos, N. Ding, M.G. Kanatzidis, Layered metal sulfides: exceptionally selective agents for radioactive strontium removal, Proc. Natl. Acad. Sci. USA 105 (2008) 3696–3699, https://doi.org/10.1073/pnas.0711528105.
[50] T. Wen, X. Wu, M. Liu, Z. Xing, X. Wang, A.-W. Xu, Efficient capture of strontium from aqueous solutions using graphene oxide–hydroxyapatite nanocomposites, Dalton Trans. 43 (2014) 7464, https://doi.org/10.1039/c3dt53591f.
[51] Y. Park, Y.-C. Lee, W.S. Shin, S.-J. Choi, Removal of cobalt, strontium and cesium from radioactive laundry wastewater by ammonium molybdophosphate–polyacrylonitrile (AMP–PAN), Chem. Eng. J. 162 (2010) 685–695, https://doi.org/10.1016/j.cej.2010.06.026.
[52] M. Lyczko, B. Wiaderek, A. Bilewicz, Separation of radionuclides from spent decontamination fluids via adsorption onto titanium dioxide nanotubes after photocatalytic degradation, Nanomaterials 10 (2020) 1553, https://doi.org/10.3390/nano10081553.
[53] A.I. Ivanets, I.L. Shashkova, N.V. Kitikova, M.V. Maslova, N.V. Mudruk, New heterogeneous synthesis of mixed Ti-Ca-Mg phosphates as efficient sorbents of ^{137}Cs, ^{90}Sr and ^{60}Co radionuclides, J. Taiwan Inst. Chem. Eng. 104 (2019) 151–159, https://doi.org/10.1016/j.jtice.2019.09.001.
[54] A.I. Orlova, Crystalline phosphates for HLW immobilization - composition, structure, properties and production of ceramics. Spark Plasma Sintering as a promising sintering technology, J. Nucl. Mater. 559 (2022), 153407, https://doi.org/10.1016/j.jnucmat.2021.153407.